Semiclassical model for thermoelectric transport in nanocomposites

Jun Zhou,[1] Xiaobo Li,[1] Gang Chen,[2] and Ronggui Yang[1,*]
[1]*Department of Mechanical Engineering, University of Colorado, Boulder, Colorado 80309, USA*
[2]*Department of Mechanical Engineering, Massachusetts Institute of Technology, Cambridge, Massachusetts 02139, USA*
(Received 28 May 2010; published 10 September 2010)

Nanocomposites (NCs) has recently been proposed and experimentally demonstrated to be potentially high-efficiency thermoelectric materials by reducing the thermal conductivity through phonon-interface scattering and possibly by increasing the Seebeck coefficient through energy-selective carrier scattering (low-energy filtering) or quantum-size effect of electrons. In this paper, we develop a Boltzmann transport equation based semiclassical electron transport model to describe the thermoelectric transport processes in semiconductor NCs. This model considers multiband transport of electrons and holes with both the intrinsic carrier scatterings and the carrier-interface scattering. A relaxation-time model is developed for carrier-interface scattering. After fitting the model with bulk thermoelectric alloys that gives reasonable material input parameters for bulk alloys, which are close to handbook values, the model is further validated by comparing the modeled thermoelectric properties with recently reported measurement values of thermoelectric properties in high efficiency NCs. The model is then applied to predict thermoelectric properties of both the particle-host-type and the particle-particle-type semiconductor NCs such as the *p*-type $(Bi_ySb_{2-y}Te_3)$-$(Bi_{0.5}Sb_{1.5}Te_3)$ NCs and the *n*-type $(Mg_2Si_yGe_{1-y})$-$(Mg_2Si_{0.6}Ge_{0.4})$ NCs. The dependence of thermoelectric transport coefficients on the size of nanoconstituent, doping concentration and temperature are studied. Our study could shed some light to optimally design high-efficiency thermoelectric NCs which could contribute to solar-thermal utilization or waste heat recovery.

DOI: 10.1103/PhysRevB.82.115308 PACS number(s): 73.63.−b, 62.23.Pq, 65.80.−g

I. INTRODUCTION

Thermoelectricity which directly converts between thermal gradients (temperature difference) and electricity is expected to play significant roles in the global energy crisis and the thermal-management challenges of high heat flux systems.[1–3] Efficiency of thermoelectric (TE) devices (refrigerator or power generator) is determined by the dimensionless figure of merit (ZT) of TE materials

$$\mathrm{ZT} = \frac{S^2\sigma T}{\kappa_c + \kappa_p}, \tag{1}$$

where S is the Seebeck coefficient, σ is the electrical conductivity, T is the absolute temperature, κ_c is the thermal conductivity due to the contribution of electrical carriers (both electrons and holes), κ_p is thermal conductivity due to the contribution of quantized lattice vibration (phonons), and $S^2\sigma$ is usually mentioned as the power factor.[4,5] The higher the ZT is, the better is the performance of a TE material or device. Apparently a high ZT material should have both high power factor $(S^2\sigma)$ and low thermal conductivity. In conventional bulk materials, the quantities S, σ, and κ_c are correlated with each other that makes the independent control of these properties very difficult. Thus the best bulk TE material stays at ZT=1 for 40 years since 1950s. The introduction of nanostructures to enhancing ZT in 1990s has revolutionized the field through quasi-independent control of S, σ, and κ_c for next generation of high-efficiency TE materials.[1] The kinetic model gives $S=\frac{1}{eT}\left[\frac{\langle E\tau\rangle}{\langle\tau\rangle}-\mu\right]$, where E is the energy of electrical carrier, τ is the relaxation time of electrical carrier, μ is the chemical potential and the bracket denotes the statistical average. Apparently the Seebeck coefficient S represents the average energy of mobile electrical carriers. Changing the density of states (DOS) of electrons or holes that are responsible for electrical current could significantly alters the Seebeck coefficient while a gain of the power factor or ZT could come from an optimal control of the DOS. Coherent control of electrons through low-dimensional quantum structures such as superlattices and nanowires (NWs) presents most obvious ways to control DOS which stimulates most of the research in superlattice[6] and NWs TE.[7–10] Doping of a TE material with resonant energy level which originates from impurity levels presents another interesting and relatively new way to engineer the shape of DOS for high efficiency TE material.[11] Filtering low-energy carriers through incoherent or random interfaces indeed presents a very promising approach for changing DOS of transporting carriers that could significantly enhance S while not requiring precise control of material structures in synthesis. While a qualitative model has been presented in early 1990s for electron filtering,[12,13] a rigorous model for the impact of energy filtering is still short of. Another more significant contributor to the recently reported high ZT materials is the reduction of lattice thermal conductivity induced by phonon-interface scattering.[1] Nanocomposite (NC) materials is indeed a material platform that could be easily synthesized to realize both low-energy electrical carrier filtering and the reduction in lattice thermal conductivity without the burden of coherent control of electrical and thermal carriers.[1]

Over the past few years, we have witnessed significant amount of works and progresses in nanostructured TE using potentially cost-effective NCs. The TE properties of various NCs materials have been reported experimentally.[14–30] For example, Poudel *et al.*[31] reported a significant increase in ZT reaching a peak about 1.4 near 373 K in *p*-type $Bi_{0.5}Sb_{1.5}Te_3$-alloy-based NCs material. All these experimental studies indicated that ZT can be enhanced through proper

tuning of the composition and the size of nanoconstituent in NCs materials in comparison with bulk alloy materials. Recently, Medlin and Snyder[32] presented a review of the studies to control and understand the formation and the transport properties of the NCs materials.

Theoretical study of TE NCs has also grown significantly over the last few years due to its importance in guiding the materials synthesis. The lattice or phonon thermal conductivity of NCs was studied and reported in a series of papers by Yang and Chen[33,34] using the phonon Boltzmann transport equation (BTE) and then using the phonon Monte Carlo simulation after realizing that the Fourier theory based heat conduction model for conventional composites could not be used to predict the thermal conductivity of NCs.[35] Similarly, theoretical models have recently been proposed to challenge the validity of using the conventional bulk TE transport model to predict electron transport properties of NCs, which was proposed by Bergman *et al.*[36,37] in 1990s using effective transport matrix and field decoupling transformation method. These new models usually introduce a carrier-interface relaxation time τ_b to account for the interface scattering experienced by carriers in NCs by assuming a given barrier height of one-dimensional rectangular potential barrier without considering the detailed band structures.[13,38–40] More recently, Minnich *et al.*[41] used the charge-trapping model to account for the interface scattering in NCs. Taking one step ahead, Faleev *et al.*[42] and Zebarjadi *et al.*[43] used the Born approximation, and the partial wave method to calculate the scattering cross section of carriers and thus the carrier-interface relaxation time when electrical carriers experience a more realistic material interface that is governed by the Poisson equation. However, this method is valid under the dilute limit, i.e., the concentration of nanoconstituent, which could be nanoparticle (NP) or NW, should be very low, so that each NP or NW can be treated independently. When the nanoconstituent concentration is high, Zebarjadi *et al.*[44] introduced an effective medium theory based on coherent potential approximation similar to that used in disorder electron systems.[45,46]

In this paper, we present a semiclassical phenomenological model to study TE transport in NCs under the framework of the Boltzmann transport theory. Comparing to the recent works, our contributions are as follows: (1) two different types of NCs are studied and compared: one is nanoconstituent embedded in a host material (matrix) and the other is an assemblage of two kinds of nanoconstituents. (2) Our model considers the transport processes in both nanoconstituent materials that makes our model to be useful for both types of NCs with a large range of volumetric fraction and the size of nanoconstituent. (3) We develop a relaxation time model for carrier-interface scattering. Furthermore, we generalize the carrier-interface scattering by introducing geometric factors that could be related to arbitrary geometry of nanostructures in NCs and thus enabling us to study the effect of nanostructure geometry on the transport properties. (4) We consider detailed shape of energy barriers by numerically solving the Poisson equation for band bending near an interface between two different materials in NCs. (5) By using the modified effective medium approximation (EMA),[47] the lattice thermal conductivity of NCs is calculated which enabled us to calculate the effective ZT of NCs. Our study could thus shed some light to optimally design high-efficiency TE NCs which could contribute to solar-thermal utilization or waste heat recovery.

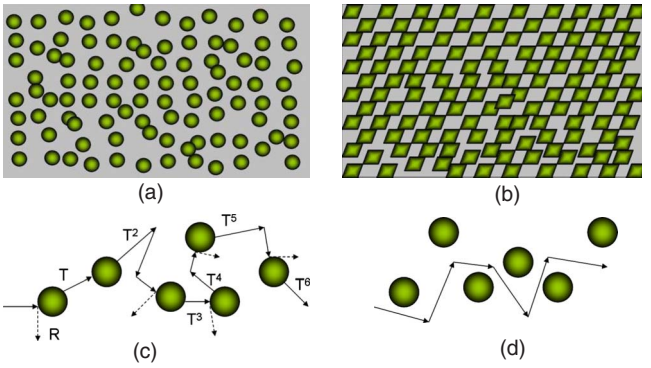

FIG. 1. (Color online) (a) Nanoconstituents (NPs or NWs) embedded in a host (matrix) material, noted as particle-host-type NCs. In this type of NCs, any two points in the matrix can be connected without encountering any nanoconstituents. (b) Mixture of different kinds of nanoconstituents, noted as particle-particle-type NCs. In this type of NCs, two arbitrary points in two separated nanostructures of the same material cannot be connected without encountering the other kind of nanoconstituent. (c) Schematic of the random trajectory of a carrier transmitting through or scattered by NPs one by one with transmission probability P and reflection probability $R=1-P$. (d) Schematic of the open path that the carrier does not meet any interfaces. This open path can exist only in particle-host-type NCs. In a particle-particle-type NCs, there is no such open path because of the absence of topological connectedness.

This paper is organized as follows. We present a Boltzmann transport model for the transport of multiband electrons and holes in Sec. II. A relaxation-time model for carrier-interface scattering is presented in Sec. III. Then we present the detailed studies of p-type $(Bi_ySb_{2-y}Te_3)$-$(Bi_{0.5}Sb_{1.5}Te_3)$ and n-type $(Mg_2Si_yGe_{1-y})$-$(Mg_2Si_{0.6}Ge_{0.4})$ NCs after briefly presenting the fitting procedures for material input parameters of the model in Sec. IV. Finally, Sec. V concludes this paper.

II. MULTIBAND CARRIER-TRANSPORT MODEL IN NC

Depending on the synthesis processes, there are generally two types of NCs with two constituent materials: NPs or NWs embedded in a host material (matrix) as shown in Fig. 1(a) and an assemblage of two kinds of NPs or NWs, as shown in Fig. 1(b).[1] The former one is called particle-host-type NCs in which there is topological connectedness (each two points in matrix could be connected without encountering any NP or NW) and the latter one is called particle-particle-type in which there is no such connectedness (two arbitrary points in two separated NP or NW of the same material cannot connect with each other without encountering a NP or NW of the other constituent material). In both types of NCs, we assume that the interaction of electrical carriers with nanostructures can be characterized by the scattering possibility which defines the carrier-interface relaxation time τ_b, without considering the quantum size effects

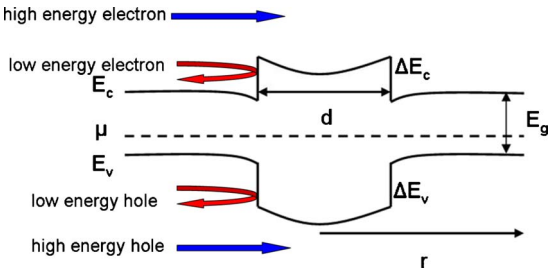

FIG. 2. (Color online) Schematic of the cross section of the band structure of NP and the filtering effect. Here $E_c(E_v)$ is the conduction (valence) band edge and $\Delta E_c(\Delta E_v)$ is the conduction (valence) band edge difference of two materials. E_g is the band gap of the matrix material, d is the size of NP, and r is the radial axe of a spherical coordinate. High-energy carriers can transport through an energy barrier and the low-energy carriers are scattered back.

on the electrical carriers. Such kind of energy-selective carrier scattering will filter the electrical carriers whose energy are lower than the barrier height (noted as E_b) while the carriers whose energy are higher than E_b can easily pass through an interface,[13] as shown in Fig. 2. Therefore, Seebeck coefficient will increase in NCs since the average entropy (or average energy) carried by electrical carriers is enhanced by energy-selective filtering effect although the electrical conductivity decreases.[12,48]

We calculate the TE transport properties in NCs under the framework of the BTE with relaxation-time approximation (RTA). The model considers electrical carriers in multiple energy bands with the Kane model. We use the Mathiessen's rule by assuming that the scattering events are independent with each other

$$\frac{1}{\tau_{i,j}^{tot}} = \frac{1}{\tau_{i,j}} + \frac{1}{\tau_{b,i,j}}, \tag{2}$$

where $\tau_{i,j}^{tot}$ is the total relaxation time, $\tau_{i,j}$ is the relaxation time of intrinsic scattering mechanisms in bulk alloys, and $\tau_{b,i,j}$ is the carrier-interface relaxation time which will be modeled in Sec. III. Here, $i=(1,2,\ldots)$ represents the index of electron bands, $j=(e,h)$ represents the electrons (e) and holes (h). When considering detailed scattering mechanisms, $\tau_{i,j}$ in Eq. (2) could be written as Eq. (3) below while the individual intrinsic scattering relaxation time in Eq. (3) will be presented in Sec. II B

$$\frac{1}{\tau_{i,j}} = \frac{1}{\tau_{i,j}^{imp}} + \frac{1}{\tau_{i,j}^{po}} + \sum_{l} \frac{1}{\tau_{i,j}^{da,l}} + \sum_{l'} \frac{1}{\tau_{i,j}^{do,l'}}, \tag{3}$$

where $\tau_{i,j}^{imp}$ is the relaxation time of carrier-impurity (imp) scattering, $\tau_{i,j}^{po}$ is from carrier-longitude polar optical (po) phonon scattering, $\tau_{i,j}^{da,l}$ is from carrier-deformation acoustic (da) phonon scattering and $\tau_{i,j}^{do,l'}$ is from carrier-deformation optical (do) phonon scattering, where l (l') denotes the different branches of deformation acoustic (optical) phonon.

Following assumptions are made for our model: (1) the nanostructures do not change the band structure remarkably and the effect of interfaces on the electrical carrier transport can be treated as a random incoherent scattering so that such a perturbation can be represented by the carrier-interface relaxation time. (2) Quantum confinement of electrons in nanoconstituents is ignored which will keep our model within the semiclassical category. This assumption is valid when the size of nanoconstituents is large. For small size, when the doping concentration inside the nanoconstituents is low that we choose in this paper, the assumption is also valid since the length of depletion layer is larger than the size of nanoconstituents that leads a smooth and flat band structure inside the nanoconstituents. (3) The interfaces between nanoconstituents are considered as a series of potential barriers.[40] When the electrical carriers travel in the NCs with random trajectories, they will meet interfaces randomly. (4) We ignore the anisotropy of all the relaxation times similar to others' work.[40,49] (5) We consider the transport probabilities in other kinds of nanoconstituent geometries to be similar to the spherical ones as we focus on the averaging effect of low-energy carrier filtering. We believe that the effective effect of different geometries with same effective barrier height could be similar. Assumptions (1) and (3) are reasonable and useful considering that the endeavor of high efficiency NCs is to pursue easy routes to synthesize high ZT TE materials[18,20] Assumptions (2), (4), and (5) are for simplicity of this model.

A. Thermoelectric transport with multiple band carriers

We consider TE transport of electrons in both the lowest conduction bands and the highest valence bands in the multiband carrier-transport model.[3] Each of these bands is considered to be N-folded degeneracy where the dispersion relations of each carrier pocket can be written using the Kane model to consider the nonparabolicity

$$\frac{\hbar^2 k_{i,j,\parallel}^2}{2m_{i,j,\parallel}^*} + \frac{\hbar^2 k_{i,j,\perp}^2}{m_{i,j,\perp}^*} = \gamma(E_{i,j}) = E_{i,j} + \frac{E_{i,j}^2}{E_g}. \tag{4}$$

Here $m_{i,j,\parallel}^*$ $(m_{i,j,\perp}^*)$ is the effective mass in a carrier pocket parallel (perpendicular) to the cleavage plane near the band edge and $k_{i,j,\parallel}$ $(k_{i,j,\perp})$ is the corresponding wave vector. It is noted that $m_{i,j}^* = (m_{i,j,\parallel}^{*2} m_{i,j,\perp}^*)^{1/3}$ is the density-of-states effective mass of each carrier pocket, and $m_{d,i,j}^* = (N)^{2/3} m_{i,j}^*$ is the density-of-states effective mass of each energy band. In order to take the nonparabolicity into account, we consider the energy term as $\gamma(E_{i,j}) = E_{i,j}(1 + E_{i,j}/E_g)$, where $E_{i,j}/E_g$ is the nonparabolicity factor which is very important for small band-gap semiconductor such as bismuth telluride TE materials, E_g is the energy gap.

The doping concentration n_d is defined here as the absolute difference between the concentrations of electrons and holes. The chemical potential μ for a fixed n_d can then be determined by

$$n_d = \left| \sum_i \frac{\sqrt{2} m_{d,i,e}^*}{\pi^2 \hbar^3} \int_0^\infty \gamma^{1/2}(E_{i,e}) \gamma'(E_{i,e}) \times \frac{1}{e^{(E_{i,e}+E_{i,e,0}-\mu+E_g)/k_B T}} dE_{i,e} - \sum_i \frac{\sqrt{2} m_{d,i,h}^*}{\pi^2 \hbar^3} \int_0^\infty \gamma^{1/2}(E_{i,h}) \gamma'(E_{i,h}) \frac{1}{e^{(E_{i,h}+E_{i,h,0}+\mu)/k_B T}} dE_{i,h} \right|, \tag{5}$$

where $\gamma'(E_{i,j})=1+2E_{i,j}/E_g$, $E_{i,j,0}$ is the band edge, k_B is the Boltzmann constant, and $\hbar$ is the Plank constant. The first term on the right in Eq. (5) is the electron concentration and the second term is the hole concentration. It is obvious that they are temperature dependent for fixed n_d.

The TE transport coefficients such as electrical conductivity σ, Seebeck coefficients S, and electronic thermal conductivity κ_c can then be calculated using the BTE under RTA. Particularly, for anisotropic materials like $Bi_{0.5}Sb_{1.5}Te_3$ alloy, the TE coefficients in different directions are not the same since $m^*_{i,j,\parallel} \neq m^*_{i,j,\perp}$, where we denote $\xi=(\parallel,\perp)$. Then the anisotropic thermal properties of each direction after considering the bipolar effect of the electrons and holes can be written as[4]

$$\sigma_\xi = \sum_j \sigma_{\xi,j}, \quad \sigma_{\xi,j} = \sum_i \frac{q_j^2}{3\pi^2 m^*_{\xi,i,j}} \left(\frac{2k_B T m^*_{d,i,j}}{\hbar^2}\right)^{3/2} L^0_{i,j}, \tag{6}$$

$$S_\xi = \sum_j \frac{S_j \sigma_{\xi,j}}{\sigma_{\xi,j}}, \quad S_j = \frac{k_B}{q_j}\left(\frac{\sum_i \frac{(m^*_{d,i,j})^{3/2}}{m^*_{\xi,i,j}} L^1_{i,j}}{\sum_i \frac{(m^*_{d,i,j})^{3/2}}{m^*_{\xi,i,j}} L^0_{i,j}} - \eta_{i,j,F}\right), \tag{7}$$

$$\kappa_{c,\xi} = \frac{\sigma_{\xi,e}\sigma_{\xi,h}}{\sigma_{\xi,e}+\sigma_{\xi,h}}(\alpha_e-\alpha_h)^2 T + \sum_j \kappa_{c,\xi,j},$$

$$\kappa_{c,\xi,j} = \sum_i \frac{k_B}{3\pi^2 m^*_{\xi,i,j}} \left(\frac{2k_B T m^*_{d,i,j}}{\hbar^2}\right)^{3/2} \times \left(L^2_{i,j} - \frac{\sum_{i'} \frac{(m^*_{d,i',j})^{3/2}}{m^*_{\xi,i',j}} L^1_{i',j}}{\sum_{i'} \frac{(m^*_{d,i',j})^{3/2}}{m^*_{\xi,i',j}} L^0_{i',j}} L^1_{i,j}\right). \tag{8}$$

Here q_j denotes the charge of carrier, $\eta_{i,j}=E_{i,j}/k_BT$, $\eta_{i,e,F}=(\mu-E_g-E_{i,e,0})/k_BT$, $\eta_{i,h,F}=(-\mu-E_{i,h,0})/k_BT$, $\eta_g=E_g/k_BT$, and $\gamma(\eta_{i,j})=\eta_{i,j}(1+\eta_{i,j}/\eta_g)$, respectively. The integrals in Eqs. (6)–(8) can be written as

$$L^n_{i,j}(T) = \int_0^\infty \eta^n_{i,j}\gamma^{3/2}(\eta_{i,j})\tau^{tot}_{i,j}\left(-\frac{\partial f_0}{\partial \eta_{i,j}}\right)d\eta_{i,j}, \tag{9}$$

where f_0 is the equilibrium Fermi-Dirac distribution.

It should be emphasized that we focus on the parallel components of TE coefficients in the rest of this paper. Therefore, we will ignore the subscript in Eqs. (6)–(8) of parallel components for presentation convenience.

B. Relaxation time of intrinsic scattering mechanisms

In TE alloys, carriers experience impurity scattering, deformation acoustic phonon-scattering, deformation optical phonon-scattering, and longitudinal polar optical phonon-scattering mechanisms. The total relaxation time of intrinsic scattering for each band $\tau_{i,j}$ in TE bulk materials can be obtained according to the Matthiessen's rule as described in Eq. (3).

The relaxation time due to ionized impurity scattering is given as[50]

$$\tau^{imp}_{i,j} = \frac{16\sqrt{2m^*_{i,j}}\pi\varepsilon_s^2}{n_{imp}Z^2e^4}\frac{\gamma^{3/2}(E_{i,j})}{\gamma'(E_{i,j})}\left[\ln(1+4k^2\iota^2) - \frac{4k^2\iota^2}{1+4k^2\iota^2}\right]^{-1}, \tag{10}$$

where $Z=2$ is the ionicity of an impurity atom we considered, ε_s is the static permittivity, n_{imp} is the impurity density, e is the charge of carrier, k is the wave vector of carrier, and ι is the screening length of screened Coulomb potential, respectively. We choose the Debye screening for convenience in this paper

$$\iota^2 = \frac{\varepsilon_s k_B T}{e^2 n_d}. \tag{11}$$

The relaxation time due to longitudinal polar optical scattering under both elastic scattering assumption (ESA) and high temperature assumption can be written as[49]

$$\tau^{po}_{i,j} = \frac{4\sqrt{2}\pi\hbar^2}{e^2 k_B T\sqrt{m^*_{i,j}}} \times \left[\frac{1}{\varepsilon_\infty}-\frac{1}{\varepsilon_s}\right]^{-1}\frac{\gamma^{1/2}(E_{i,j})}{\gamma'(E_{i,j})}\left[1-\frac{1}{4k^2\lambda^2}\ln(1+4k^2\lambda^2)\right]^{-1}, \tag{12}$$

where ε_∞ is the high-frequency permittivity.

The relaxation time due to deformation potential of acoustic and optical phonon scattering under ESA can be written as[50]

$$\tau^{da,l}_{i,j} = \frac{\pi\rho c_l^2\hbar^4}{\sqrt{2}\varphi_1^2 k_B T m^{*3/2}_{i,j}}\frac{1}{\gamma^{1/2}(E_{i,j})\gamma'(E_{i,j})}, \tag{13}$$

$$\tau^{do,l'}_{i,j} = \frac{\hbar^2 a^2\rho(\hbar\omega_{l'})^2}{\sqrt{2}\pi\varphi_2^2 k_B T m^{*3/2}_{i,j}}\frac{1}{\gamma^{1/2}(E_{i,j})\gamma'(E_{i,j})}, \tag{14}$$

where ρ is the mass density, φ_1 (φ_2) is the acoustic (optical) deformation potential coupling constant, a is the lattice constant, c_l is the sound velocity of lth branch of acoustic phonon mode, and $\omega_{l'}$ is the frequency of l'th branch of optical phonon mode, respectively. Here, we ignore the screening effect of deformation potential of acoustic and optical phonon scatterings.

III. RELAXATION-TIME MODEL FOR CARRIER-INTERFACE SCATTERING

The relaxation time is the average flight time between two scatterings events. Assuming that the carrier-interface scattering is independent from other scattering mechanisms, then the relaxation time for carrier-interface scattering τ_b can be written as $\lambda_\alpha/v_\alpha+\lambda_\beta/v_\beta$ for particle-host-type NCs and $\lambda'_\alpha/v_\alpha+\lambda'_\beta/v_\beta$ for particle-particle-type NCs, where v is the velocity of carrier, $\lambda(\lambda')$ is the average free path length[51] in

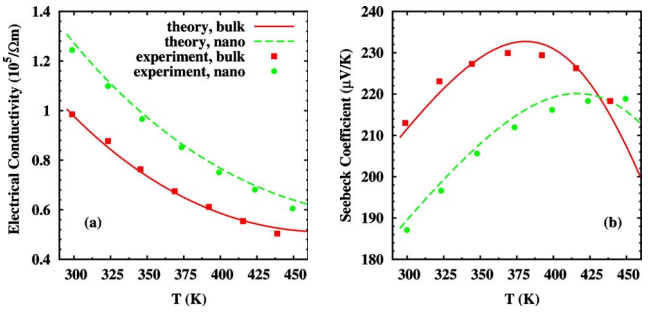

FIG. 3. (Color online) Calculated temperature-dependent TE transport properties for the state-of-the-art *p*-type $Bi_{0.5}Sb_{1.5}Te_3$ alloy and its corresponding NCs, in comparison with the recently reported experimental data in Ref. 31: (a) electrical conductivity. (b) Seebeck coefficient. See Table I for fitting parameters.

each constituent material, and α and β are the indexes of different constituent materials in NCs. For convenience, we ignore the band index (i,j) in the following discussion.

The average free path length λ could be evaluated based on the average distance L between two successive boundaries/interfaces and the carrier transmission probability P through a potential barrier. When the carriers travel in NCs with random trajectories, they will encounter the interfaces between constituent materials randomly. The carriers transmit through the potential barrier of the interfaces one by one with transmission probability P, or be scattered away by these barriers with reflection coefficient $1-P$ as shown in Fig. 1(c).[51] If an electrical carrier does not meet any potential barriers during its random trajectory, we called this trajectory as open path as shown in Fig. 1(d).

In the following, we try to relate the average free path length λ with the average distance between two successive interfaces L and the transmission probability P, and then to obtain the expression for the relaxation time τ_b of carrier-interface scattering. We denote L in the matrix material as L_α and L in the nanoconstituent material as L_β in a particle-host-type NCs. If we consider there are an arbitrary number n of carriers at the starting point of random trajectory, the free path length of open path for these carriers is nL_α. Then nP carriers will pass through the first barrier with free path length nPL_α in matrix and free path length nPL_β in nanoconstituent. At this, nP^i carriers will pass through the ith barrier with free path length nP^iL_α in matrix and free path length nP^iL_β in nanoconstituent. The total free path lengths are $nL_\alpha(1+P+\cdots+P^i)$ in matrix and $nL_\beta(P+\cdots+P^i)$ in nanoconstituent. Let i to be infinite, one can get $\lambda_\alpha=\frac{L_\alpha}{1-P}$ and $\lambda_\beta=\frac{L_\beta P}{1-P}$. The extra P in λ_β is coming from the absence of open path. Therefore, the relaxation time due to interface scattering is

$$\tau_b = \frac{L_\alpha}{v_\alpha}\frac{1}{1-P} + \frac{L_\beta}{v_\beta}\frac{P}{1-P}, \tag{15}$$

where v_α is the velocity of the carrier in matrix and v_β is the velocity in nanoconstituents.

In a particle-particle-type NCs, we denote L in the two constituents L'_α and L'_β, respectively. Because of the absence

TABLE I. Parameters used to calculate the transport coefficients for *p*-type $Bi_{0.5}Sb_{1.5}Te_3$ alloy and its NCs materials.

Parameters	Fitted value	Reference	Parameters	Fitted value	Reference
m_e^*/m_0	0.248	0.06[a]	$\hbar\omega$ (meV)	6.2–14.9	6.1[a]
		~0.25 [b]			6.2–14.9[c,d]
m_h^*/m_0	0.277	0.08[a]	φ_1 (eV)	9.5	35[a]
		0.3[e]	φ_2 (eV)	9.5	40[a]
		~0.29 [b]			
$\lvert n_d\rvert$ (cm^{-3})	5×10^{19}		ε_s (ε_0) [f]	260	400[a]
	7.05×10^{19} [g]				75–290[c]
					36.5–168[e]
n_{imp} (cm^{-3})	1.33×10^{19}		ε_∞ (ε_0) [f]	30	69.8[a]
	1.5×10^{19} [g]				50–85[c]
					29.5–53[e]
a (nm)	1.045	1.045[a]	c_l (m/s)	1870–2950	1870–2950[c]
E_g (eV)	$0.221-1.5\times10^{-4}$ T	$0.13-1.08\times10^{-4}$ T [a]	ρ (g/cm^3)	7.86	7.86[a,c]
	$0.216-1.2\times10^{-4}$ T [g]	0.13–0.14(293 K) [c]			
		0.21–0.28(300 K) [e]			

[a] Bi_2Te_3 (Ref. 49).
[b] $Bi_{0.5}Sb_{1.5}Te_3$ (Ref. 53).
[c] Bi_2Te_3 (Ref. 54).
[d] We consider 12 modes for optical phonon.
[e] Sb_2Te_3 (Ref. 54).
[f] ε_0 is the permittivity of free space.
[g] Parameters used while fitting to NCs materials.

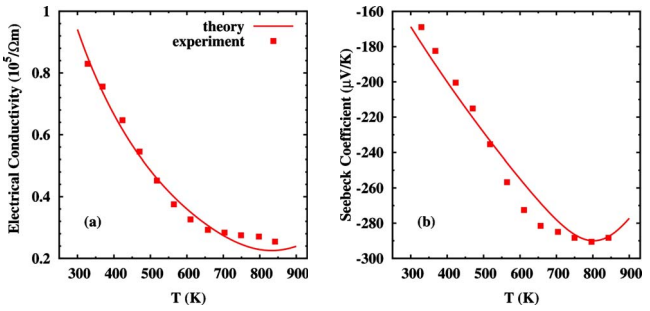

FIG. 4. (Color online) Calculated temperature-dependent TE transport properties for the *n*-type $Mg_2Si_{0.6}Ge_{0.4}$ alloy, in comparison with experimental data in Ref. 55: (a) electrical conductivity. (b) Seebeck coefficient. See Table II for fitting parameters.

of connectedness, there is no open path as shown in Fig. 1(d). The average free path length λ in each particle constituent can be written as $\lambda'_\alpha = \frac{L'_\alpha P}{1-P}$ and $\lambda'_\beta = \frac{L'_\beta P}{1-P}$. The relaxation time for the carrier-interface scattering in a particle-particle-type NCs would thus be slightly different from that in a particle-host-type NCs and can be written as

$$\tau_b = \frac{L'_\alpha}{v_\alpha}\frac{P}{1-P} + \frac{L'_\beta}{v_\beta}\frac{P}{1-P}. \tag{16}$$

By comparing Eqs. (15) and (16), we can easily find that $\tau_b \to \infty$ when $P \to 1$ for both two cases that means the high-energy electrons transport through the nanoconstituents transparently. We can also find that $\tau_b \to \frac{L_\alpha}{v_\alpha}$ in Eq. (15) and $\tau_b \to 0$ in Eq. (16) when $P \to 0$ that means all the low energy electrons are blocked unless there is open path.

A. Calculation of average distance *L*

In this section, we consider the relation between *L* which is the average distance between two successive scatterings and macroscopic parameters that can be controlled in experiment such as the volumetric fraction of the nanoconstituents *x* and the characteristic size of nanoconstituents *d* (*d* is diameter for spherical NP and cylindrical NP, side length for cubic NP and cuboid NW, and so on.) by introducing an intermediate quantity-average area per unit volume θ, which is the surface-volume ratio that controls effectiveness of carrier-interface scattering.

For a particle-host-type NCs

$$x = Ad^3/D^3, \tag{17}$$

$$\theta = Bd^2/D^3, \tag{18}$$

where *D* is the size of unit volume, and *A* and *B* are geometric factors. With the above, we can easily relate the surface-volume ratio with the characteristic size and the volume ratio as $\theta = \frac{Bx}{Ad}$. L_α in the matrix material is proportional to $1-x$ and L_β in the particle material is proportional to *x*. Both L_α and L_β are inversely proportional to θ. They can then be written as

$$L_\alpha = \left(\frac{\theta}{1-x}\right)^{-1} = \frac{Ad(1-x)}{Bx}, \quad L_\beta = \left(\frac{\theta}{x}\right)^{-1} = \frac{Ad}{B}. \tag{19}$$

The geometry factors in Eq. (17) and (18) denote the shape of a nanoconstituent material. We present here the determination of *A* and *B* in some typical nanostructures such as spherical and cubic NPs, cylindrical and cuboid NWs. For a spherical NP, the volume of the particle is $\pi d^3/6$ and the surface area is πd^2, therefore $A = \pi/6$, $B = \pi$, and $A/B = 1/6$. For a cubic NP, the volume of the particle is d^3 and the surface area is $6d^2$, therefore $A = 1$, $B = 6$, and $A/B = 1/6$. For a cylindrical NW, the volume of NW is $\pi\varsigma d^3/4$, where ς is the ratio of the length of the wire to the diameter *d*, and the surface area is $\pi d^2(\varsigma + 1/2)$, therefore $A = \pi\varsigma/4$ and $B = \pi(\varsigma + 1/2)$. If an NW is long and thin, in other words $\varsigma \gg 1$, then $A/B \sim 1/4$. For a cuboid NW, the volume of the NW is ςd^3, and the surface area is $4d^2(\varsigma + 1/2)$, therefore $A = \varsigma$ and $B = 4(\varsigma + 1/2)$. If $\varsigma \gg 1$, one can get $A/B \sim 1/4$. In

TABLE II. Parameters used to calculate the transport coefficients for *n*-type $Mg_2Si_{0.6}Ge_{0.4}$ alloy (Ref. 55).

Parameters	Fitted value	Reference	Parameters	fitted value	Reference
m_e^*/m_0	0.219	0.46,0.53[a]	$\hbar\omega$ (meV)	33	32–43.7[a,b]
		0.18[c]			25.6–33.7[b,c]
m_h^*/m_0	0.707	0.87,2.2[a]	φ_1 (eV)	9	
		0.31[c]	φ_2 (eV)	9	
$\lvert n_d \rvert$ (cm^{-3})	0.93×10^{19}		ε_s (ε_0)	18.8	18.8,20[a]
n_{imp} (cm^{-3})	6.64×10^{17}		ε_∞ (ε_0)	13.3	13.3[a]
					13.9[c]
a (nm)	6.35	6.338[a]	c_l (m/s)	4970–7680	4970–7680[a]
		6.393[c]			3800–6300[c]
E_g (eV)	$0.788-4\times10^{-4}$ T	$0.78-5\times10^{-4}$ T [a]	ρ (g/cm^3)	1.88	1.88[a]
		$0.74-2\times10^{-4}$ T [c]			

[a]Mg_2Si (Ref. 54).
[b]We consider six modes for optical phonon.
[c]Mg_2Ge (Ref. 54).

TABLE III. Material properties for phonon transport, c_v is the specific heat.

Material	Model	κ_p (W/mK)	c_v (10^6J/m^3 K)	V (m/s)	MFP (nm)
Bi_2Te_3	Debye	1.1	1.22	2950	0.91
	Dispersion	1.1	0.5	212	31
Sb_2Te_3	Debye	0.9	1.32	3000	0.68
	Dispersion	0.9	0.53	200	25.4

short, the influence of the geometry can be summarized into the geometric ratio A/B for any arbitrary geometry following the similar consideration as above examples.

For a particle-particle-type NCs, both constituents are NPs or NWs. It is convenient to consider constituent α as nanoconstituent when constituent β can be considered as matrix similar to the particle-host-type. Then we can define the size of nanoconstituent as d_α, the size of the unit volume as D_α and the geometric factors as A_α, B_α. We can also consider constituent β as nanoconstituent and α as matrix, then we can define the size of nanoconstituent as d_β, the size of the unit volume as D_β, and the geometric factors as A_β, B_β. As the unit total volume and the unique interface between the two components, we can write the relations similar to Eqs. (17) and (18)

$$x = A_\alpha d_\alpha^3/D_\alpha^3, \quad 1-x = A_\beta d_\beta^3/D_\beta^3, \tag{20}$$

$$\theta = B_\alpha d_\alpha^2/D_\alpha^3 = B_\beta d_\beta^2/D_\beta^3. \tag{21}$$

Equations (20) and (21) give a strong restriction of the formation of particle-particle-type of NCs. Similar to Eq. (19), L'_α and L'_β can be written as

$$L'_\alpha = \frac{A_\alpha d_\alpha}{B_\alpha}, \quad L'_\beta = \frac{1-x}{x} L'_\alpha. \tag{22}$$

We note that the geometry of nanoconstituents in a practical NCs could be very complicated and sometimes could be anisotropic in terms of crystal orientation for anisotropic materials. However, geometric factors as discussed above could help to generalize the averaging effects of interfaces into simple formulas as shown in Eq. (19) and (22). This simplification gives us a convenient way to study the filtering effect of interfaces in NCs not only made of simple NP geometry but also that of the random geometry nanoconstituents. In this work, we choose $A/B=A_\alpha/B_\alpha=1/6$ throughout the paper for convenience.

B. Calculation of carrier transmission probability P

The carrier transmission probability P through energy barrier is a function of the carrier energy, the detailed shape (height and width) of each potential barrier. For calculating P, we investigate the band diagram near the interface, i.e., the shape of potential barrier. Band bending near an interface is determined by the electrostatic force due to the carrier redistribution, carrier trapping, and the intrinsic band edge difference of two constituent materials. For simplicity of this work, we just consider spherical inclusion as an example and do not consider the carrier trapping near the interface. As mentioned earlier, a spherical shape approximation is reasonable since we are interested only in the average interface effects. The carrier trapping and interface oxidization are very important for the barrier height and is critical for controlling the TE transport properties. However for modeling efforts, considering carrier trapping is not a significant challenge by adding an additional term in the Poisson equation. In the spherical coordinate, one can solve the Poisson equation to obtain electrostatic potential $\phi(r)$ and carrier distribution $n(r)$ self-consistently

$$\frac{d^2}{dr^2} r\phi(r) = r\frac{n(r)}{\varepsilon}, \tag{23}$$

where ε is the static permittivity and r is the radial variable. We solve this second order differential equation using fourth-order Runge-Kutta and shooting methods with the boundary conditions $\phi(\infty)=0$, and $\phi(0)=0$ as well as the continuity condition at interface. According to the calculated $\phi(r)$ and the intrinsic band edge difference of conduction band ΔE_c and valence band ΔE_v, the typical band bending of both conduction band and valence band can be obtained as shown in Fig. 2. As expected, the barrier height of conduction (valence) band is partly determined by $\Delta E_c(\Delta E_v)$ and partly determined by the band bending due to depletion effect near interface, when carrier trapping is not considered. It is well known that ΔE_c is equal to the difference of electron affinities of two constituents of NCs, and $\Delta E_v=\Delta E_g-\Delta E_c$, where ΔE_g is the band gap difference of two constituents. The difference of conduction bands ΔE_c and valence bands ΔE_v can be tuned by the chemistry stoichiometry. Finally, the transmission probability P through the potential barriers of both conduction bands and valence bands are calculated by solving the one-dimensional Schrödinger equation numerically[52] using the finite difference method. Here, we approximate the sphere by a planar interface.

IV. RESULTS AND DISCUSSION

The model presented in Secs. II and III gives a tool for calculating TE transport properties of NCs. In this section, we first compare our theoretical calculations with the experimental data of $Bi_{0.5}Sb_{1.5}Te_3$ alloy and $Mg_2Si_{0.6}Ge_{0.4}$ alloy to obtain the fitting parameters of these alloys. $Bi_{0.5}Sb_{1.5}Te_3$ alloy is currently the state-of-the-art p-type commercial TE material for temperature control and thermal-management application around room temperature. $Mg_2Si_{0.6}Ge_{0.4}$ alloy is

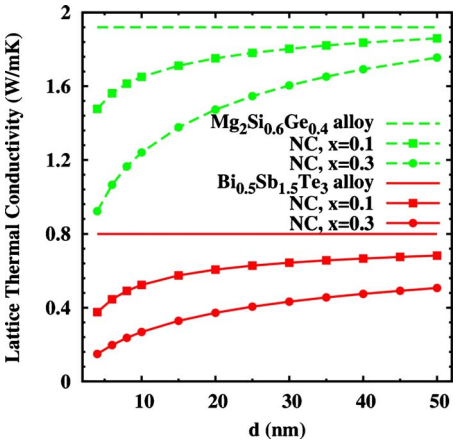

FIG. 5. (Color online) Size dependence of the lattice thermal conductivity of $Bi_{0.5}Sb_{1.5}Te_3$ and $Mg_2Si_{0.6}Ge_{0.4}$ alloys and their NCs with different volumetric fractions.

a medium temperature range TE material which has significant impacts on waste heat recovery and solar thermal utilization.[38] The fitting parameters are in good agreement with known values reported in handbooks and references, which gives us strong confidence that the multiband Boltzmann transport model can capture TE transport in alloys. After the correct input parameters are identified for TE alloys, we incorporate the relaxation-time model for interface-scattering to model TE properties of recently reported high-efficiency $Bi_{0.5}Sb_{1.5}Te_3$-based NCs. Our theoretical model agrees well with the experimental data and helps to give good explanation for recently observed ZT enhancement in NCs. We then present the calculated TE properties of $Bi_{0.5}Sb_{1.5}Te_3$-alloy and $Mg_2Si_{0.6}Ge_{0.4}$-alloy-based TE NCs of both particle-host and particle-particle types.

A. Model validation

We verify our model through a two-step process by comparing the theoretical calculation with the state-of-the art alloys (p-type $Bi_{0.5}Sb_{1.5}Te_3$ and n-type $Mg_2Si_{0.6}Ge_{0.4}$) and then the recently reported high-efficiency TE NCs made of p-type $Bi_{0.5}Sb_{1.5}Te_3$. Figure 3 shows the comparison of the calculation results of our multiband TE transport model with the experimental data of p-type $Bi_{0.5}Sb_{1.5}Te_3$ alloy reported by Poudel *et al.* in Ref. 31. The lowest two conduction bands and the highest two valence bands with zero energy difference between their band edges,[49] i.e., $E_{1,e,0}=E_{2,e,0}$ and $E_{1,h,0}=E_{2,h,0}$, are considered. The degeneracy of each band is set to be $N=6$. Our calculation results fit well the reported experimental data from 300 to 450 K. Table I presents the fitting parameters for our model to capture the experimental value. Apparently, these fitting parameters are in good agreement with reported values in handbooks and other references.

After proper material parameters are identified for both TE alloys, we incorporate the relaxation time model for carrier-interface scattering as presented in Sec. III to model the TE transport properties of recently reported high-efficiency bismuth-telluride alloy-based NCs: the particle-particle-type $(Bi_{0.14}Sb_{1.86}Te_3)$-$(Bi_{0.5}Sb_{1.5}Te_3)$ NCs materials. As shown in Fig. 3, our calculation results agree well with the experimental data by choosing an effective barrier height $E_b \sim 0.05$ eV, the average size of particles $d=20$ nm as reported in Ref. 31, and the volumetric fraction of nanoconstituent $x=0.06$ as fitting parameters. Other fitting parameters can be found in Table I. The material properties of the nanoconstituent material are chosen to be the same as the matrix material as shown in Table I. Apparently these fitting parameters for NCs show that our multiband Boltzmann transport model along with the newly developed relaxation time model can capture TE transport in NCs.

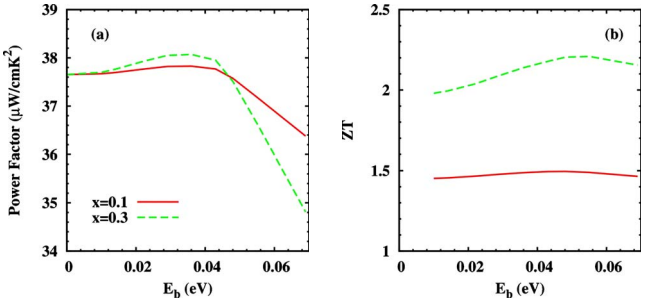

FIG. 6. (Color online) The dependence of power factor and ZT on the effective energy barrier height for particle-host-type NCs with $Bi_{0.5}Sb_{1.5}Te_3$ as matrix material for different volumetric fractions. The calculations use $T=373$ K, $n_d=6n_0$, and $n_0=10^{19}/\text{cm}^3$ as input parameters.

In Fig. 4, we also compare our modeling results with the experimental data of n-type $Mg_2Si_{0.6}Ge_{0.4}$ alloy reported by Akasaka *et al.* in Ref. 55. $Mg_2Si_{0.6}Ge_{0.4}$ alloy is an important nontoxic light-weight TE material that has high ZT over medium temperature range (700–1000 K), which is attracting more attentions these days for waste heat recovery. The lowest two conduction bands and the highest two valence bands are considered. The energy difference between the first and the second conduction bands[54] is chosen to be 0.07 eV, i.e., $E_{2,e,0}-E_{1,e,0}=0.07$ eV while the energy difference between the two valence bands is zero, *i.e.*, $E_{1,h,0}=E_{2,h,0}$. The degeneracy of each band is chosen to be $N=2$. The calculation results fit the experimental data very well within a very large temperature range, from 300 to 900 K. Table II presents all the fitting material input parameters that are in good agreement with values reported in handbooks and other references.

The model validation steps reported above not only give us great confidence that our multiband Boltzmann transport model with carrier-interface scattering relaxation time can capture TE transport in both n- and p-type alloys and NCs but also help to identify the correct set of material input parameters for further investigation on TE-alloy-based NCs as presented in the rest of this paper.

B. Phonon thermal conductivity of NCs

The thermal conductivity of NCs has the contribution from both electrons and phonons. The electronic thermal conductivity can be calculated using Eq. (8) as discussed in Sec. II A. In general, the thermal conductivity has a similar

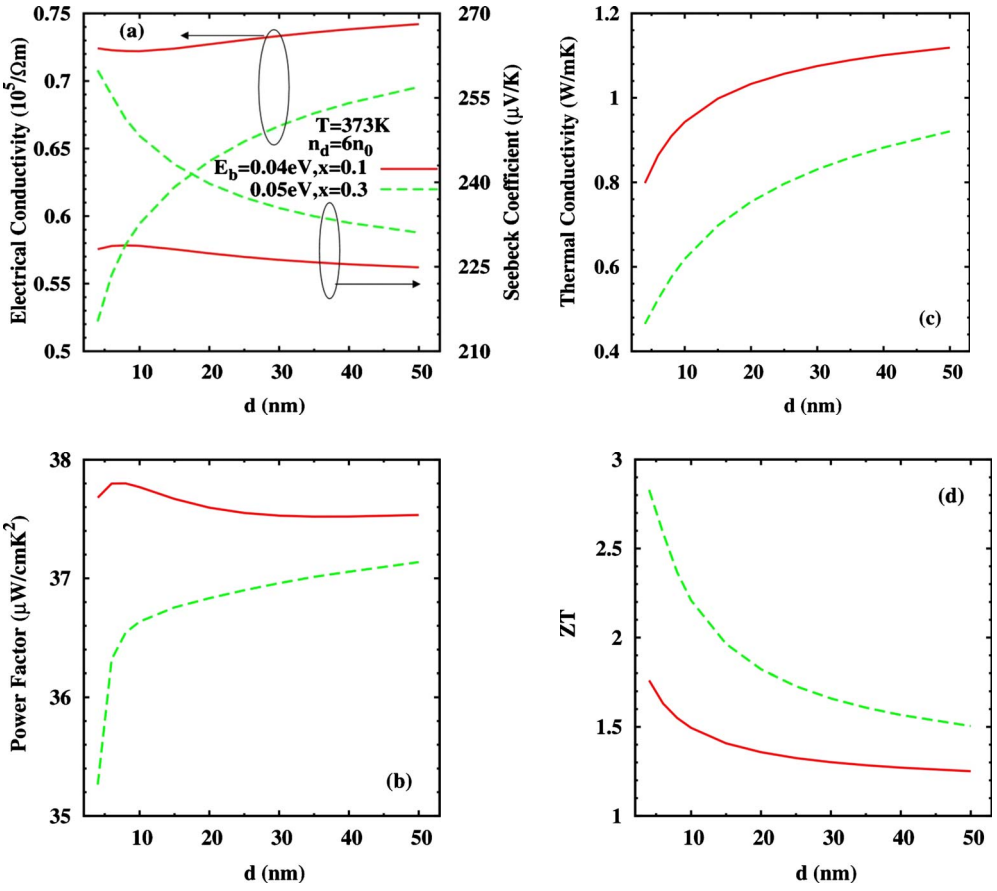

FIG. 7. (Color online) Size dependence of (a) electrical conductivity and Seebeck coefficient, (b) power factor, (c) total thermal conductivity, and (d) ZT for particle-host-type NCs with $Bi_{0.5}Sb_{1.5}Te_3$ as matrix for different barrier heights E_b and volumetric fractions x. The calculations use $T=373$ K, $n_d=6n_0$, and $n_0=10^{19}/\mathrm{cm}^3$ as input parameters. For comparison, the electrical conductivity in the base $Bi_{0.5}Sb_{1.5}Te_3$ alloy material is $0.761\times10^5/\Omega$ m, the Seebeck coefficient is 222.5 μ V/K, the power factor is 37.1 μW/cm K^2, total thermal conductivity is 1.25 W/mK, and the ZT is 1.13.

dependence on doping concentration and characteristic size of nanostructures as electrical conductivity of NCs since the Wiedemann-Franz law still holds for NCs. It is well known as of today that thermal conductivity of nanostructured materials could be significantly reduced due to the scattering of phonons at interfaces between the lattice-mismatched materials when the characteristic size of the nanostructure is smaller than the phonon mean free path (MFP),[56] which is estimated for tens to hundreds of nanometers for most of semiconductor materials. As discussed in the introduction of this paper, much work including has been done on modeling and simulation of the thermal conductivity of semiconductor NCs.[33,34] Here we used the modified EMA (Ref. 47) to model the phonon thermal conductivity of NCs as a function of the size nanoconstituents and the volumetric fraction of the particle. Details can be found in Appendix. In this model, the key input is the estimation of the MFP and the group velocity of heat-carrying phonons. Following the references, we estimated the MFP and the group velocity of the heat-carrying phonons by approximating the dispersion with a sine function instead of the Debye model which assumes a linear-dispersion relationship between the phonon frequency and the wave vector. Table III lists the estimated values for the phonon MFP, group velocity (v) and specific heat (C_v) for the material constituents of the NCs studied in this article. After a reasonable estimation of the phonon properties, the effective thermal conductivity of the constituent materials is estimated based on the relative contributions from the intrinsic thermal conductivity and thermal boundary resistance. With the newly obtained effective thermal conductivity of the constituent materials, the effective medium theory is used to calculate the effective thermal conductivity of the NCs. This model has been verified by comparing the results with computationally intensive simulations of phonon BTE.[33] Results of the size-dependent thermal conductivity are presented in Fig. 5 for particle-host-type NCs made of p-type $Bi_{0.5}Sb_{1.5}Te_3$-alloy and n-type $Mg_2Si_{0.6}Ge_{0.4}$-alloy with different volumetric fractions of their corresponding alloy nanoconstituents.

C. BiSbTe alloy-based NCs

We study the particle-host-type NCs based on the p-type BiSbTe alloy material in this section. The matrix material used is the state-of-the-art p-type room temperature TE material with optimal ZT: $Bi_{0.5}Sb_{1.5}Te_3$. The inputs for material properties are those verified fitting parameters listed in Table I. For the particle inclusions, we chose $Bi_ySb_{2-y}Te_3$, where y

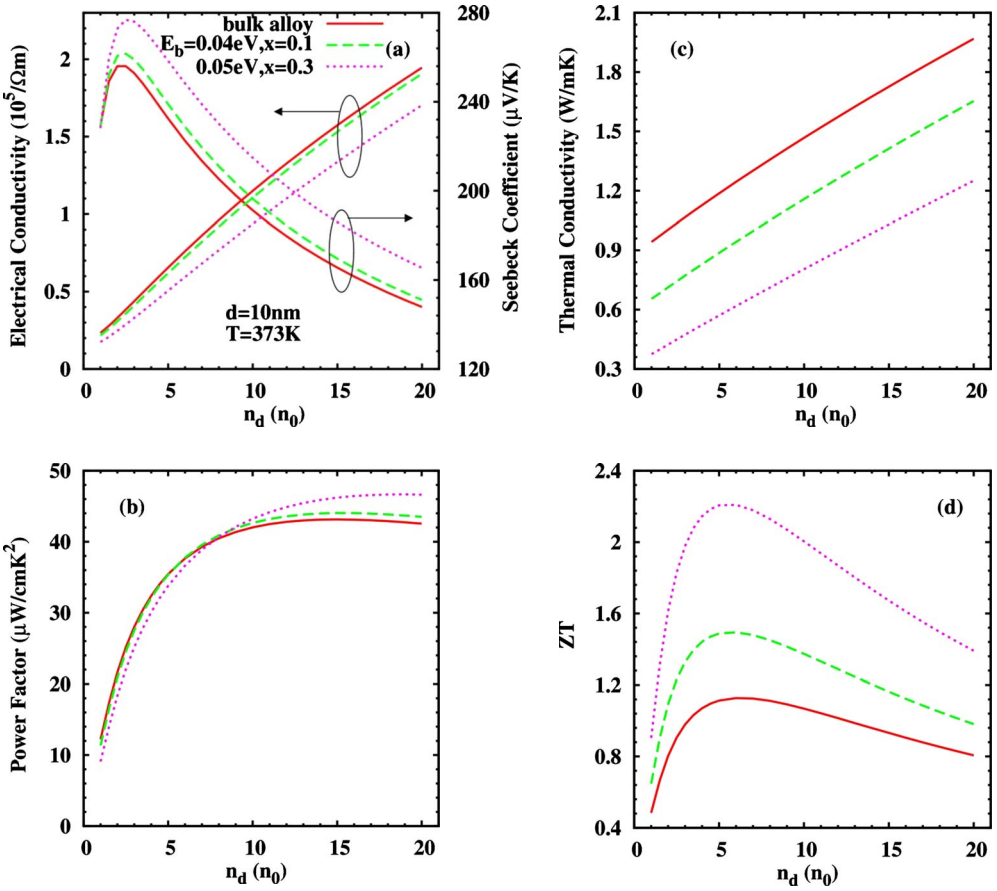

FIG. 8. (Color online) Carrier density dependence of (a) electrical conductivity and Seebeck coefficient, (b) power factor, (c) total thermal conductivity, and (d) ZT for particle-host-type NCs with $Bi_{0.5}Sb_{1.5}Te_3$ as matrix material for different barrier heights E_b and volumetric fractions x in comparison with $Bi_{0.5}Sb_{1.5}Te_3$ bulk alloy. The calculations use $T=373$ K and $d=10$ nm as input parameters, $n_0=10^{19}/cm^3$.

is an adjustable parameter with $y<0.5$. Accordingly, a positive band alignment can be given as $\Delta E_v=0.07(1-2y)$ eV where the difference of valence band edges between Sb_2Te_3 and $Bi_{0.5}Sb_{1.5}Te_3$ is assumed to be 0.07 eV. The material properties in the nanoconstituent are chosen to be the same as the matrix. Other input parameters used in this subsection are $T=373$ K, $n_d=6n_0$, and $d=10$ nm unless specified and $n_0=10^{19}$ cm^{-3} is used throughout the paper.

Barrier height is a key parameter for the TE transport in NCs. There exists an optimal barrier height for interface filtering of low-energy electrons as a result of the competition between the decrease in the electrical conductivity and the increase in the Seebeck coefficient in NCs. Figure 6 shows the power factor and ZT of $(Bi_ySb_{2-y}Te_3)_x$-$(Bi_{0.5}Sb_{1.5}Te_3)_{1-x}$ as a function of E_b for two different volumetric fraction x. Clearly, the optimum barrier height for maximum power factor is around 0.03–0.04 eV and it is around 0.05 eV for maximum ZT. Using the simple barrier height estimation discussed earlier in this section, we find that the optimal nanoconstituent material should be $Bi_{0.14}Sb_{1.86}Te_3$ (with $y=0.14$) when not considering the charge trapping at interfaces. Figure 6 also shows that the optimum power factors does not change much with x for the same particle size $d=10$ nm. However, ZT could be changed dramatically from ZT=2 to ZT=1.45 from $x=0.3$ to $x=0.1$. This indeed confirms the importance of thermal conductivity reduction in TE NCs research. Of course, the practical challenge in TE NCs synthesis is to make a controllable interface between particles that are not easy to oxidize and have controllable electrostatic barrier.

Figure 7 shows the size dependence of electrical conductivity, Seebeck coefficient, power factor, total thermal conductivity, and ZT for two different $(Bi_ySb_{2-y}Te_3)_x$-$(Bi_{0.5}Sb_{1.5}Te_3)_{1-x}$ NCs with volumetric fractions, $x=0.1$ (with optimum $E_b=0.04$ eV when $y=0.21$) and $x=0.3$ (with optimum $E_b=0.05$ eV when $y=0.14$). For a fixed size d, large x means more interfaces in the NCs, which results in higher Seebeck coefficient and lower electrical conductivity for $x=0.3$ than that for $x=0.1$ NCs as shown in Fig. 7(a). For a fixed x, electrical conductivity increases and the Seebeck coefficient decreases with the increase of size d since less interfaces are involved. However, such a change in electrical conductivity and Seebeck coefficient is significant only for $x=0.3$ [Fig. 7(a)] while the power factor of NCs with both $x=0.1$ and $x=0.3$, shown in Fig. 7(b), does not change dramatically with the size d. Figure 7(c) shows that the total thermal conductivity which is a summation of both electronic and phononic thermal conductivity, as discussed in Sec. IV B, decreases with the increase of x. The thermal conductivity reduction is rather dramatic for small size of nanoconstituent. For example with $x=0.3$, the total thermal conductivity for $d=5$ nm case is about 50% of $d=50$ nm

case. Overall the TE ZT can be greatly enhanced due to the significant reduction of the total thermal conductivity and a competitive power factor with optimized parameters, as shown in Fig. 7(d). The maximum ZT could reach 2.8 when $d=4$ nm and $x=0.3$. It is important that our model is valid only when d is much larger than the Fermi wavelength which is about $1/\sqrt[3]{12\pi^2 n_d} \sim 1$ nm in this material.

Figure 8 shows the dependence on the doping concentration of the TE transport coefficients for $(Bi_ySb_{2-y}Te_3)_x$-$(Bi_{0.5}Sb_{1.5}Te_3)_{1-x}$ with characteristic particle size of 10 nm in comparison with the bulk $Bi_{0.5}Sb_{1.5}Te_3$ alloy. In the range of the plotted doping concentration, NCs has a reduced electrical conductivity and an enhanced Seebeck coefficient. However, the overall change in power factor is not significant, as shown in Fig. 8(b). The peak of the power factor has a slight shift to a higher n_d while the amplitude increase a little for large n_d and decrease a little for small n_d in NCs compared to the bulk alloy. Apparently the total thermal conductivity increases linearly with the doping concentration since the electronic and phononic contributions to the total thermal conductivity are usually comparable for high-efficiency TE materials. A significant reduction in phononic thermal conductivity due to the increase in phonon-interface scatting results in the decrease of the overall thermal conductivity as shown in Fig. 8(c). Such a reduction in thermal conductivity induces significant increase in the TE ZT for NCs with $x=0.3$ [Fig. 8(d)]. Interestingly the maximum ZT for optimized TE NCs appears at around the same doping concentration as that of optimal bulk alloy, at $6n_0$.

Figure 9 shows the optimized ZT for particle-host-type $(Bi_ySb_{2-y}Te_3)_x$-$(Bi_{0.5}Sb_{1.5}Te_3)_{1-x}$ NCs with a characteristic particle size of 10 nm and different x (here y is chosen for an optimal barrier height as identified in Fig. 6, without considering carrier trapping at interfaces). Also shown in the Fig. 6 is the experimental value of reported high ZT particle-particle-type $Bi_{0.5}Sb_{1.5}Te_3$-alloy-based NCs. The maximum value of ZT near 373 K could reach *2* with $d=10$ nm, $E_b=0.05$ eV, and $x=0.3$. The optimal temperatures for all cases are within 350–400 K which is important for application of NCs in solar-thermal utilization or waste heat recovery. Our results also show that there are still much rooms to improve ZT of $Bi_{0.5}Sb_{1.5}Te_3$-alloy-based NCs beyond the exciting results published by Poudel *et al.*[31] by tuning the size of nanostructures and the doping concentration. We also comment that although the thermal conductivity reduction is the obvious mechanisms for ZT enhancement in NCs, significant challenges in developing high-efficiency TE NCs is to remain the power factor considering the carrier trapping at interface and oxidation can easily occur in the synthesis processes.

D. MgSiGe alloy-based NCs

As mentioned earlier, MgSiGe alloy based TE material are attracting more attentions for medium temperature range waste heat harvesting. Here we study the particle-host-type NCs based on the n-type MgSiGe alloy material in this section. The matrix material used is the n-type $Mg_2Si_{0.6}Ge_{0.4}$ TE alloy that has an optimal ZT. The input for material properties are those verified during the fitting process as listed in Table II. For the particle inclusions, we chose $Mg_2Si_yGe_{1-y}$, where y is an adjustable stochoimetry parameter with $y<0.6$. Accordingly, a positive band alignment can be given as $\Delta E_c=0.1(1-5y/3)$ eV where the difference of conduction-band edges between Mg_2Ge and $Mg_2Si_{0.6}Ge_{0.4}$ is assumed to be 0.1 eV. The material properties in the nanoconstituent are chosen to be the same as the matrix. Other input parameters used in this section are $T=800$ K, $n_d=3n_0$, and $d=10$ nm unless specified.

Figure 10 shows the power factor and ZT of $(Mg_2Si_yGe_{1-y})_x$-$(Mg_2Si_{0.6}Ge_{0.4})_{1-x}$ as a function of E_b for different volumetric fractions x. The optimum barrier height for maximum power factor is around 0.04–0.06 eV and it is around 0.08 eV for maximum ZT. Using the simple barrier height estimation discussed earlier, we find the optimal nanoconstituent material should be $Mg_2Si_{0.12}Ge_{0.88}$ (with $y=0.12$). Figure 10 also shows that the optimum power factors does not change much with x for the same particle size $d=10$ nm. However, ZT could be changed dramatically from ZT=1.16 to ZT=0.92 from $x=0.3$ to $x=0.1$ due to a much drastic thermal conductivity reduction in NCs with $x=0.3$.

Comparing Fig. 10 with Fig. 6, we can see that the optimum barrier height of n-type MgSiGe–alloy-material-based NCs is larger than the p-type BiSbTe–alloy-based NC. This is because of the much higher operation temperature of the MgSiGe–alloy-based TE NCs. At a higher operating temperature, more carriers are distributed on the states with higher energy. Therefore, a higher barrier height is needed for effective filtering.

Figure 11 shows the size dependence of electrical conductivity, Seebeck coefficient (note it is negative for n-type materials), power factor, total thermal conductivity, and ZT for the two different $(Mg_2Si_yGe_{1-y})_x$-$(Mg_2Si_{0.6}Ge_{0.4})_{1-x}$ NCs with volumetric fractions, $x=0.1$ (with optimum $E_b=0.05$ eV when $y=0.3$) and $x=0.3$ (with optimum $E_b=0.08$ eV when

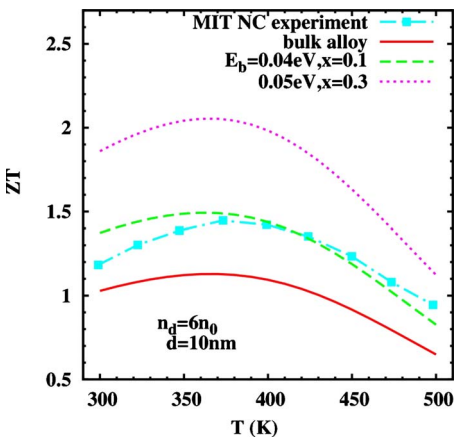

FIG. 9. (Color online) Temperature dependence of ZT for particle-host-type NCs with $Bi_{0.5}Sb_{1.5}Te_3$ as matrix material for barrier heights E_b and volumetric fractions x in comparison with $Bi_{0.5}Sb_{1.5}Te_3$ bulk alloy. We choose $n_d=6n_0$, $n_0=10^{19}/\mathrm{cm}^3$, and $d=10$ nm as input parameters since it is the optimal case we found in Fig. 7(d). The dashed curve is the reported high ZT experimental data from Ref. 31.

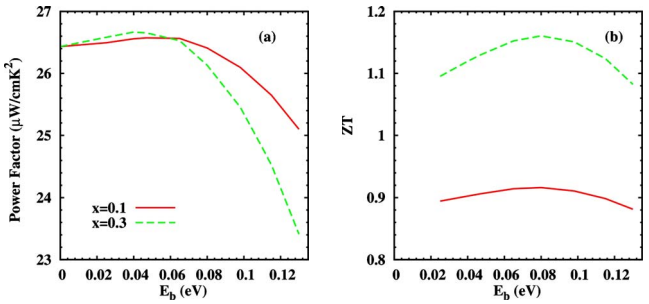

FIG. 10. (Color online) Barrier height dependence of power factor and ZT for particle-host-type NCs with $Mg_2Si_{0.6}Ge_{0.4}$ as matrix materials for different volumetric fractions x. The calculations use $T=800$ K, $n_d=3n_0$, and $n_0=10^{19}/\mathrm{cm}^3$ as input parameters.

$y=0.12$). For a fixed size d, large x results in higher Seebeck coefficient and lower electrical conductivity as shown in Fig. 11(a). For a fixed volumetric percentage x, electrical conductivity increases and the Seebeck coefficient decreases with the increase in d. Such a change is more significant for $x=0.3$ [Fig. 11(a)] while the power factor of NCs with both $x=0.1$ and $x=0.3$ does not change remarkably with d as shown in Fig. 11(b). Figure 11(c) shows that the total thermal conductivity decreases with the increase in x and the reduction in thermal conductivity is dramatic smaller size nanoconstituent. Finally, Fig. 11(d) shows that the TE ZT can be greatly enhanced due to the significant reduction in the total thermal conductivity and a competitive power factor with optimized parameters. The maximum ZT could be *1.5* for $d=4$ nm and $x=0.3$.

Figure 12 shows the dependence on the doping concentration of the TE transport coefficients for $(Mg_2Si_yGe_{1-y})_x$-$(Mg_2Si_{0.6}Ge_{0.4})_{1-x}$ NCs with $d=10$ nm in comparison with the bulk $Mg_2Si_{0.6}Ge_{0.4}$ alloy. Figure 12(a) shows that NCs have a reduced electrical conductivity and an enhanced Seebeck coefficient. However, the overall change in power factor is not remarkable as shown in Fig. 12(b). The peak of power factor has a shift to a higher n_d while the amplitude increase a little for large n_d and decrease a little for small n_d in comparison with the bulk alloy. In Fig. 12(b), the peak of power factor shift to higher n_d. The decrease of overall thermal conductivity due to the increase of phonon-interface scattering is shown in Fig. 12(c). Such a reduction in thermal conductivity induces significant increase in the TE ZT for NCS with $x=0.3$ [Fig. 12(d)]. The maximum value of ZT for the optimized TE NCs appears at a higher doping concentration, $2.8n_0$, than that of optimal bulk alloy, $2n_0$.

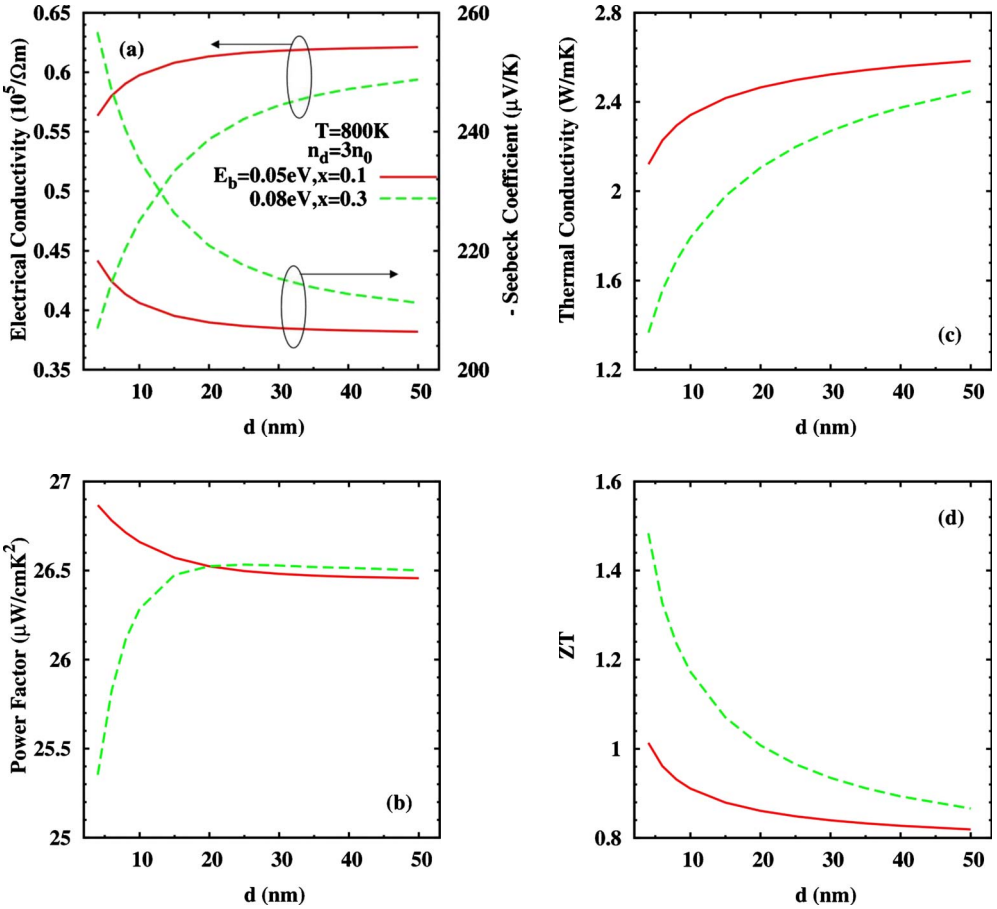

FIG. 11. (Color online) Size dependence of (a) electrical conductivity and Seebeck coefficient, (b) power factor, (c) total thermal conductivity, and (d) ZT for particle-host-type NCs with $Mg_2Si_{0.6}Ge_{0.4}$ as matrix materials for different barrier heights E_b and volumetric fractions x. The calculations use $T=800$ K, $n_d=3n_0$, and $n_0=10^{19}/\mathrm{cm}^3$ as input parameters. For comparison, the electrical conductivity in the base $Mg_2Si_{0.6}Ge_{0.4}$ alloy material is $1.14\times10^5/\Omega$ m, the Seebeck coefficient is 153 μV/K, the power factor is 26.6 μW/cm K^2, total thermal conductivity is 3.32 W/mK, and the ZT is 0.64.

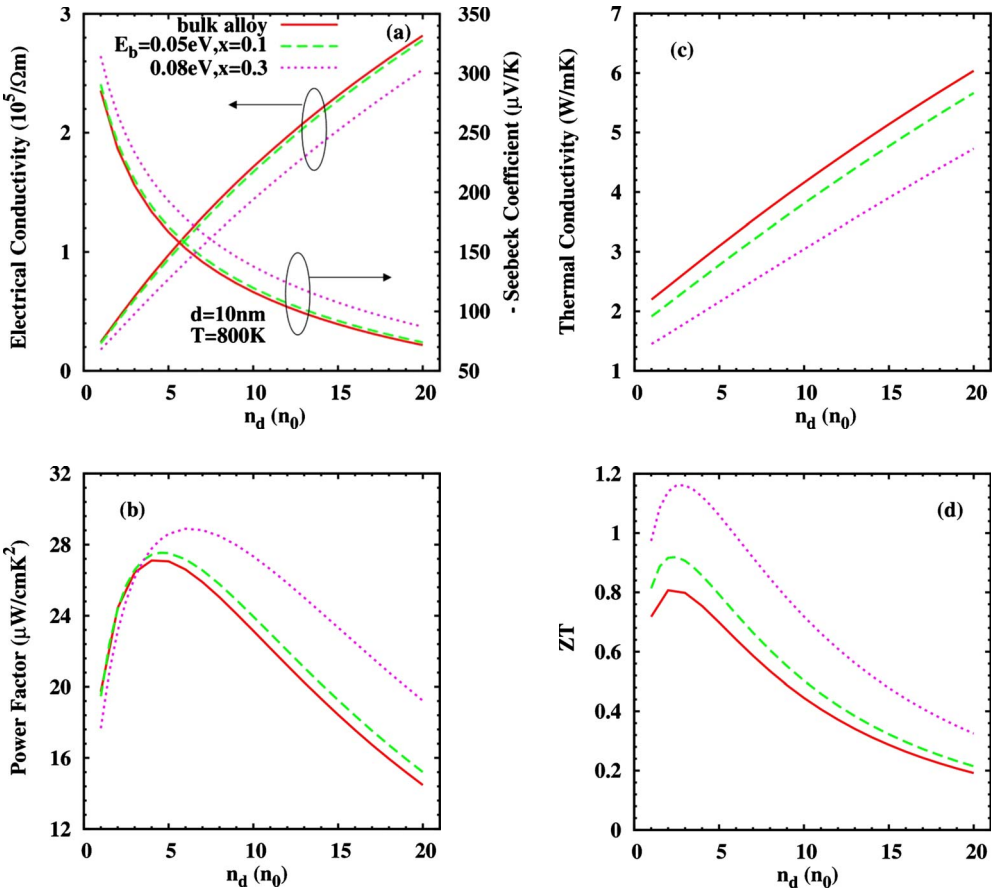

FIG. 12. (Color online) Carrier density dependence of (a) electrical conductivity and Seebeck coefficient, (b) power factor, (c) total thermal conductivity, and (d) ZT for particle-host-type NCs with $Mg_2Si_{0.6}Ge_{0.4}$ as matrix material for different barrier heights E_b, and volumetric fractions x. The calculations use $T=800$ K and $d=10$ nm as input parameters, $n_0=10^{19}/\mathrm{cm}^3$.

Figure 13 shows the temperature dependence of the optimal ZT for particle-host-type $(Mg_2Si_yGe_{1-y})_x$-$(Mg_2Si_{0.6}Ge_{0.4})_{1-x}$ NCs with $d=10$ nm and different volumetric fraction x (Here y is chosen for an optimal barrier height as identified in Fig. 10). The maximum value of ZT near 950 K could reach 1.22 with $d=10$ nm, $E_b=0.08$ eV, and $x=0.3$. The optimal temperatures for all cases are within 900–1000 K which is good for application of NCs in waste heat recovery.

E. Comparison of TE performance for particle-host and particle-particle types of NCs

We study the difference between the particle-particle-type and particle-host-type NCs in this section. Figure 14 shows the electrical conductivity, Seebeck coefficient, and power factor of these two kinds of $(Bi_ySb_{2-y}Te_3)_x$-$(Bi_{0.5}Sb_{1.5}Te_3)_{1-x}$ NCs with $x=0.3$ and optimal $E_b=0.05$ eV when $y=0.14$. The input parameters are $A/B=1/6$ and $d=10$ nm for particle-host-type NCs, $A_\alpha/B_\alpha=1/6$ and $d_\alpha=10$ nm for particle-particle-type NCs.

Figure 14 shows that the filtering effect of low-energy carriers in particle-particle-type NCs are much stronger than that in the particle-host-type NCs under the same set of input parameters. The reduction in electrical conductivity and the enhancement of Seebeck coefficient are more significant for the particle-particle-type NCs due to the fact that there is no open path for the low-energy carriers to go around the potential barriers in particle-particle-type NCs. This could be understood by the relaxation-time model obtained earlier. Equation (15) always gives a larger than that from Eq. (16) as $P<1$. In other words, low energy carriers are filtered more effectively by particle-particle-type NCs than that by particle-host-type NCs. Figure 14 also shows that the power factor of particle-particle-type NCs is a little smaller than particle-host-type NCs for low doping concentration case and a little larger for high doping concentration case. It is because that the reduction in electrical conductivity is larger than the enhancement of Seebeck coefficient when the doping concentration is low and the reduction in electrical conductivity is smaller than the enhancement of Seebeck coefficient when the doping concentration is high. For the optimal doping we obtained $(6n_0)$ in Fig. 8(d), the power factor of the particle-particle-type NCs is about 3% higher than that of the particle-host-type NCs. Tian and Yang[57] showed in an earlier work that thermal conductivity in a particle-particle-type NCs could be only slightly more than half the particle-host-type NCs with a same characteristic size. We thus expect that a particle-particle-type NCs material could offer much higher efficiency than that of a particle-host-type NCs

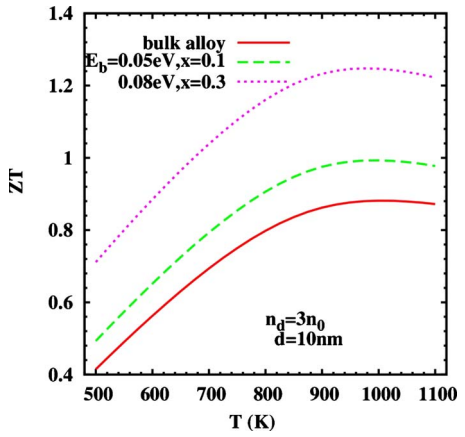

FIG. 13. (Color online) Temperature dependence of ZT for particle-host-type NCs with $Mg_2Si_{0.6}Ge_{0.4}$ as matrix materials for different barrier heights E_b and volumetric fractions x.

with the same characteristic size due to much stronger interface scattering on electrons and phonons.

V. CONCLUSIONS

We develop a multiband Boltzmann transport equation-based semiclassical model to study the TE transport properties of both particle-host-type and particle-particle-type semiconductor NCs. A relaxation-time model for electrical carrier-interface scattering is developed to account for the filtering effect of low-energy electrons on transport properties. After fitting the model with bulk TE alloys that gives reasonable adjusting parameters for bulk alloys, which are close to handbook values, the model is further validated by comparing the modeled TE properties with recently reported measurement value of TE properties in NCs. The model is then applied to predict TE properties of both the particle-host-type and the particle-particle-type semiconductor NCs such as *p*-type $(Bi_ySb_{2-y}Te_3)$-$(Bi_{0.5}Sb_{1.5}Te_3)$ and *n*-type $(Mg_2Si_yGe_{1-y})$-$(Mg_2Si_{0.6}Ge_{0.4})$. The dependence of TE transport coefficients on the size of nanoconstituents, doping concentration, and temperature are studied. We found that the TE ZT can be enhanced remarkably in NCs materials according. The reduction in thermal conductivity is the major mechanism together with a slightly changed power factor. We also point out that a particle-particle-type NCs material could offer much higher efficiency than that of a particle-host-type NCs with the same characteristic size due to much stronger interface scattering on electrons and phonons.

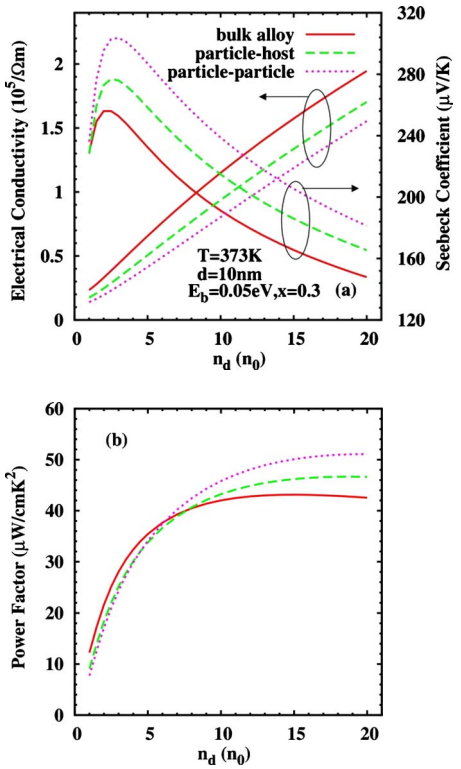

FIG. 14. (Color online) Comparison of carrier density dependence of (a) electrical conductivity and Seebeck coefficients, and (b) power factor, for particle-host-type NCs and particle-particle-type NCs. $n_0=10^{19}/cm^3$.

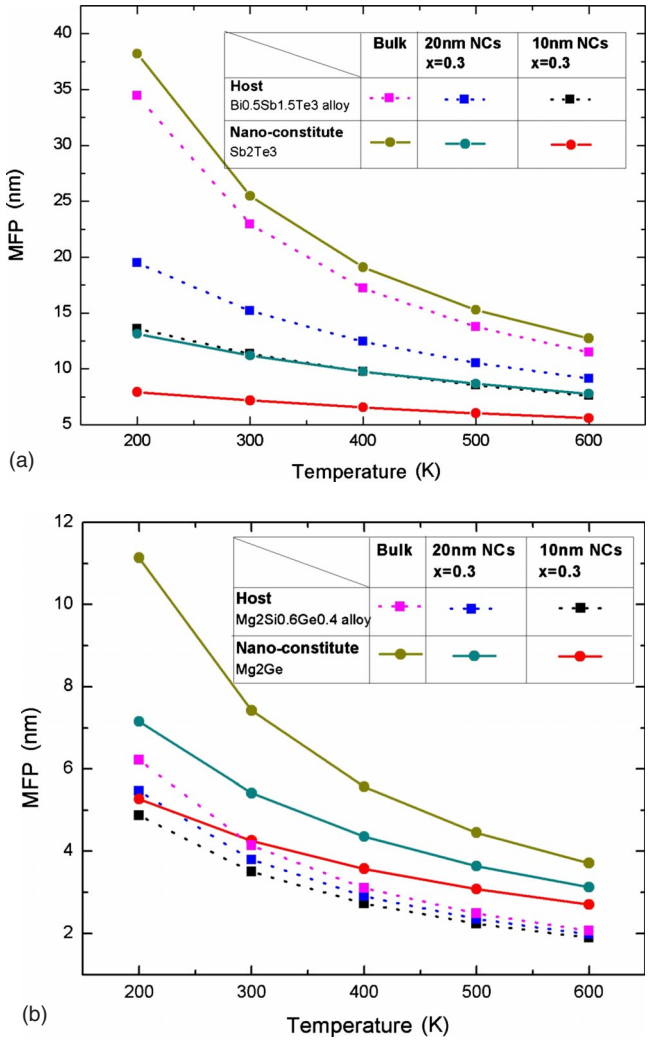

FIG. 15. (Color online) Temperature dependence of MFP in (a) $Bi_{0.5}Sb_{1.5}Te_3$-based NCs and (b) $Mg_2Si_{0.6}Ge_{0.4}$-based NCs in both the host materials and nanoconstituents in NCs with $d=10$ and 20 nm, and the corresponding bulk materials.

ACKNOWLEDGMENTS

The authors would like to thank Wei Wang for the valuable discussions. This work is supported by AFOSR (DCT Grant No. FA9550-08-1-0078 and MURI Grant No. FA9550-06-1-0326) and NSF (Grants No. CMMI 0729520 and No. CBET 0846561). G. Chen acknowledges DOE BESEFRC.

APPENDIX: ESTIMATION OF PHONON MEAN-FREE PATH

Modified effective medium model is applied to calculate the effective thermal conductivity of nanocomposites. Phonon thermal conductivity reduction is mainly due to the MFP change in nanocomposites. In this model, the MFP change has been considered for both host and particles by applying the Matthiessen's rule, i.e., the following two equations are used for the calculation of effective MFP of host and particles in nanocomposites, respectively:

$$\frac{1}{\Lambda_{eff,h}} = \frac{1}{\Lambda_{b,h}} + \frac{\Phi}{4},$$

$$\frac{1}{\Lambda_{eff,p}} = \frac{1}{\Lambda_{b,p}} + \frac{1}{d},$$

where $\Lambda_{eff,h}$ and $\Lambda_{eff,p}$ are effective MFP for host and particles in nanocomposites; $\Lambda_{b,h}$ and $\Lambda_{b,p}$ are the bulk MFP for the host and particle materials; and Φ is defined as the interface density (particle to host) and d is the particle diameter.

By approximating the dispersion with a sine function, temperature-dependent MFP is calculated from the temperature-dependent lattice thermal conductivity data. Then the temperature-dependent effective MFP of both host and particles can be obtained with the above equations. The results are shown in Fig. 15. For nanocomposites made from the *p*-type $Bi_{0.5}Sb_{1.5}Te_3$ alloy and *n*-type $Mg_2Si_{0.6}Ge_{0.4}$ alloy, we can see that if the particle size is much smaller than the MFP of the bulk (10 nm particle size in the *p*-type $Bi_{0.5}Sb_{1.5}Te_3$ alloy), the effective MFP of the host and particle are less sensitive to temperature; on the other hand if the particle size is comparable to the MFP of the bulk (the *n*-type $Mg_2Si_{0.6}Ge_{0.4}$-alloy figure), the effective MFP shows strong temperature dependence.

*Author to whom correspondence should be addressed; ronggui.yang@colorado.edu

[1] M. S. Dresselhaus, G. Chen, M. Y. Tang, R. G. Yang, H. Lee, D. Z. Wang, Z. F. Ren, J. P. Fleurial, and P. Gogna, Adv. Mater. **19**, 1043 (2007).

[2] G. J. Snyder and E. S. Toberer, Nature Mater. **7**, 105 (2008).

[3] T. M. Tritt, in *Semiconductors and Semimetals*, edited by T. M. Tritt (Academic Press, San Diego, 2001), Vols. 69-71.

[4] H. J. Goldsmid, *Thermoelectric Refrigeration* (Plenum Press, New York, 1964).

[5] D. W. Rowe, in *Thermoelectric Handbook: Macro to Nano*, edited by D. M. Rowe (CRC Press, New York, 2006).

[6] R. Venkatasubramanian, E. Siivola, T. Colpitts, and B. O'Quinn, Nature (London) **413**, 597 (2001).

[7] A. I. Hochbaum, R. Chen, R. D. Delgado, W. Liang, E. C. Garnett, M. Najarian, A. Majumdar, and P. Yang, Nature (London) **451**, 163 (2008).

[8] A. I. Boukai, Y. Bunimovich, J. Tahir-Kheli, J.-K. Yu, W. A. Goddard Iii, and J. R. Heath, Nature (London) **451**, 168 (2008).

[9] Y.-M. Lin and M. S. Dresselhaus, Phys. Rev. B **68**, 075304 (2003).

[10] J. Heremans, C. M. Thrush, Y.-M. Lin, S. Cronin, Z. Zhang, M. S. Dresselhaus, and J. F. Mansfield, Phys. Rev. B **61**, 2921 (2000).

[11] J. P. Heremans, V. Jovovic, E. S. Toberer, A. Saramat, K. Kurosaki, A. Charoenphakdee, S. Yamanaka, and G. J. Snyder, Science **321**, 554 (2008).

[12] B. Y. Moizhes and V. A. Nemchinsky, *Proceedings of the 11th International Conference on Thermoelectrics* (University of Texas Press, University of Texas, Arlington, TX, 1992).

[13] Y. I. Ravich, in *CRC Handbook of Thermoelectrics*, edited by D. M. Rowe (CRC Press, Boca Raton, 1995).

[14] N. Gothard, X. Ji, J. He, and T. M. Tritt, J. Appl. Phys. **103**, 054314 (2008).

[15] M. R. Dirmyer, J. Martin, G. S. Nolas, A. Sen, and J. V. Badding, Small **5**, 933 (2009).

[16] D. G. Ebling, A. Jacquot, H. Bottner, L. Kirste, J. Schmidt, and M. Aguirre, J. Electron. Mater. **38**, 1450 (2009).

[17] N. Mingo, D. Hauser, N. P. Kobayashi, M. Plissonnier, and A. Shakouri, Nano Lett. **9**, 711 (2009).

[18] G. Joshi, H. Lee, Y. C. Lan, X. W. Wang, G. H. Zhu, D. Z. Wang, R. W. Gould, D. C. Cuff, M. Y. Tang, M. S. Dresselhaus, G. Chen, and Z. F. Ren, Nano Lett. **8**, 4670 (2008).

[19] G. H. Zhu, H. Lee, Y. C. Lan, X. W. Wang, G. Joshi, D. Z. Wang, J. Yang, D. Vashaee, H. Guilbert, A. Pillitteri, M. S. Dresselhaus, G. Chen, and Z. F. Ren, Phys. Rev. Lett. **102**, 196803 (2009).

[20] J. Martin, G. S. Nolas, W. Zhang, and L. Chen, Appl. Phys. Lett. **90**, 222112 (2007).

[21] K. Kishimoto, K. Yamamoto, and T. Koyanagi, Jpn. J. Appl. Phys., Part 1 **42**, 501 (2003).

[22] J. P. Heremans, C. M. Thrush, and D. T. Morelli, J. Appl. Phys. **98**, 063703 (2005).

[23] J. P. Heremans, C. M. Thrush, and D. T. Morelli, Phys. Rev. B **70**, 115334 (2004).

[24] W. Kim, J. Zide, A. Gossard, D. Klenov, S. Stemmer, A. Shakouri, and A. Majumdar, Phys. Rev. Lett. **96**, 045901 (2006).

[25] B. Zhang, J. He, X. Ji, T. M. Tritt, and A. Kumbhar, Appl. Phys. Lett. **89**, 163114 (2006).

[26] X. Ke, C. Chen, J. Yang, L. Wu, J. Zhou, Q. Li, Y. Zhu, and P. R. C. Kent, Phys. Rev. Lett. **103**, 145502 (2009).

[27] J. L. Mi, X. B. Zhao, T. J. Zhu, and J. P. Tu, Appl. Phys. Lett. **91**, 172116 (2007).

[28] Y. Q. Cao, X. B. Zhao, T. J. Zhu, X. B. Zhang, and J. P. Tu, Appl. Phys. Lett. **92**, 143106 (2008).

[29] X. Shi, W. Zhang, L. D. Chen, and C. Uher, Int. J. Mater. Res. **99**, 638 (2008).

[30] T. Ikeda, E. S. Toberer, V. A. Ravi, G. J. Snyder, S. Aoyagi, E. Nishibori, and M. Sakata, Scr. Mater. **60**, 321 (2009).

[31] B. Poudel, Q. Hao, Y. Ma, Y. C. Lan, A. Minnich, B. Yu, X. Yan, D. Z. Wang, A. Muto, D. Vashaee, X. Y. Chen, J. M. Liu, M. S. Dresselhaus, G. Chen, and Z. F. Ren, Science **320**, 634 (2008).
[32] D. L. Medlin and G. J. Snyder, Curr. Opin. Colloid Interface Sci. **14**, 226 (2009).
[33] R. G. Yang and G. Chen, Phys. Rev. B **69**, 195316 (2004).
[34] R. G. Yang, G. Chen, and M. S. Dresselhaus, Phys. Rev. B **72**, 125418 (2005).
[35] M. S. Jeng, R. G. Yang, D. Song, and G. Chen, J. Heat Transfer **130**, 042410 (2008).
[36] D. J. Bergman and O. Levy, J. Appl. Phys. **70**, 6821 (1991).
[37] D. J. Bergman and L. G. Fel, J. Appl. Phys. **85**, 8205 (1999).
[38] S. J. Thiagarajan, W. Wang, and R. G. Yang, in *Annual Review of Nano Research*, edited by G. Z. Cao, Q. F. Zhang, and C. J. Brinker (World Scientific, Singapore, 2009), p. 447.
[39] J. Martin, L. Wang, L. D. Chen, and G. S. Nolas, Phys. Rev. B **79**, 115311 (2009).
[40] A. Popescu, L. M. Woods, J. Martin, and G. S. Nolas, Phys. Rev. B **79**, 205302 (2009).
[41] A. J. Minnich, H. Lee, X. W. Wang, G. Joshi, M. S. Dresselhaus, Z. F. Ren, G. Chen, and D. Vashaee, Phys. Rev. B **80**, 155327 (2009).
[42] S. V. Faleev and F. Leonard, Phys. Rev. B **77**, 214304 (2008).
[43] M. Zebarjadi, K. Esfarjani, A. Shakouri, J.-H. Bahk, Z. Bian, G. Zeng, J. Bowers, H. Lu, J. Zide, and A. Gossard, Appl. Phys. Lett. **94**, 202105 (2009).
[44] M. Zebarjadi, K. Esfarjani, A. Shakouri, Z. X. Bian, J. H. Bahk, G. H. Zeng, J. Bowers, H. Lu, J. Zide, and A. Gossard, J. Electron. Mater. **38**, 954 (2009).
[45] P. Soven, Phys. Rev. **156**, 809 (1967).
[46] D. W. Taylor, Phys. Rev. **156**, 1017 (1967).
[47] A. Minnich and G. Chen, Appl. Phys. Lett. **91**, 073105 (2007).
[48] T. E. Humphrey, M. F. O'Dwyer, and H. Linke, J. Phys. D **38**, 2051 (2005).
[49] B. L. Huang and M. Kaviany, Phys. Rev. B **77**, 125209 (2008).
[50] B. R. Nag, *Electron Transport in Compound Semiconductors* (Springer-Verlag, Berlin, 1980).
[51] S. B. A. Atakulov and A. N. Shamsiddnov, Solid State Commun. **56**, 215 (1985).
[52] S. Datta, *Electronic Transport in Mesoscopic Systems* (Cambridge University Press, Cambridge, 1995).
[53] M. Stordeur, in *CRC Handbook of Thermoelectrics*, edited by D. M. Rowe (CRC Press, Boca Raton, 1995), p. 250.
[54] *Non-Tetrahedrally Bonded Elements and Binary Compounds I*, Landolt-Börnstein Vol. III/41C, edited by O. Madelung (Springer-Verlag, Berlin, 1998).
[55] M. Akasaka, T. Iida, K. Nishio, and Y. Takanashi, Thin Solid Films **515**, 8237 (2007).
[56] G. Chen, D. Borca-Tascuic, and R. G. Yang, in *Encyclopedia of Nanoscience and Nanotechnology*, edited by H. S. Nalwa (American Scientific Publisher, Valencia, CA, 2004), Vol. 7, p. 429.
[57] W. Tian and R. Yang, J. Appl. Phys. **101**, 054320 (2007).